ARTICLES
https://doi.org/10.1038/s41566-021-00906-8

nature photonics

Two-step absorption instead of two-photon absorption in 3D nanoprinting

Vincent Hahn[1,2]✉, Tobias Messer[1], N. Maximilian Bojanowski[2], Ernest Ronald Curticean[3], Irene Wacker[4], Rasmus R. Schröder[3,4], Eva Blasco[2,4,5] and Martin Wegener[1,2]

The quadratic optical nonlinearity arising from two-photon absorption provides the crucial spatial concentration of optical excitation in three-dimensional (3D) laser nanoprinting, with widespread applications in technical and life sciences. Femtosecond lasers allow for obtaining efficient two-photon absorption but are accompanied by a number of issues, including higher-order processes, cost, reliability and size. Here we introduce two-step absorption replacing two-photon absorption as the primary optical excitation process. Under suitable conditions, two-step absorption shows the same quadratic optical nonlinearity as two-photon absorption. We present a photoresist system based on a photoinitiator supporting two-step absorption, a scavenger and a well-established triacrylate. We show that this system allows for printing state-of-the-art 3D nanostructures and beyond. In these experiments, we use ~100 μW optical power from an inexpensive, compact continuous-wave semiconductor laser diode emitting at 405 nm wavelength. Our work opens the door to drastic miniaturization and cost reduction of 3D laser nanoprinters.

In her PhD thesis, Marie Göppert-Mayer brought two-photon absorption to light[1]. In a two-photon absorption process (illustrated in Fig. 1), the light field induces a state in between the ground state and a relevant excited state of a quantum system, for example, a molecule. This induced state (Fig. 1b, dashed white line), also known as the dressed state in quantum optics[2], is commonly referred to as a virtual state. This state really exists, but only as long as the light field is switched on. When using a laser pulse, the virtual-state lifetime is determined by the pulse duration. Intuitively, the first photon induces the transition of an electron from the ground state to the virtual state, from which the second photon induces the transition to the excited state.

Today, two-photon absorption processes are crucial in multiphoton optical microscopy[3,4] and multiphoton optical lithography[5–7], both of which have been commercially available for many years. Multiphoton optical lithography has become a well-established method to fabricate three-dimensional (3D) structures from the nanoscale to the microscale[8–11]. In 3D optical lithography (also known as direct laser writing or 3D laser nanoprinting[12,13]), two-photon absorption leads to a scaling of the photoinitiator transition rate and hence of the exposure dose proportional to I^2, that is, the light intensity squared[7]. Critically, this quadratic nonlinearity suppresses unavoidable lateral and axial tails of the diffraction-limited laser focus and thereby warrants the crucial concentration of the excitation and the following chemical reaction along all three spatial directions. Importantly, one-photon absorption alone without additional nonlinearities cannot fundamentally provide this concentration in the making of arbitrary 3D structures[14]. To obtain efficient two-photon absorption, mode-locked pico- or femtosecond laser sources are routinely used. On diffraction-limited focusing, peak intensities in the range of $I = 10^{12}\,\mathrm{W\,cm^{-2}}$ and the corresponding photon irradiance of $3 \times 10^{31}\,\mathrm{s^{-1}\,cm^{-2}}$ (at a wavelength of 800 nm) provide appreciably large effective cross sections in the range of 10^{-19}–$10^{-20}\,\mathrm{cm^2}$, depending on the photoinitiator molecule[14–16].

Although being a well-established technology, using femtosecond lasers to obtain efficient two-photon absorption in 3D laser nanoprinting has a number of conceptual and practical drawbacks. First, when increasing the laser power from the point of sufficient polymer crosslinking upwards, micro-explosions occur[17] due to the onset of three- and four-photon absorption processes and beyond, leading to the unwanted population of high-energy electron states. Typically, the laser power at which micro-explosions occur is less than an order of magnitude above the writing point[18]. Sometimes, the process window is even as small as 10% (ref. [18]). Small pollutants or dirt microparticles in the photoresist can trigger micro-explosions even at the writing point. Such events render entire time-consuming 3D printing jobs useless. Second, the required femtosecond laser oscillators still cost tens of thousands of euros. Third, the femtosecond laser and its supply take up a considerable volume fraction of the overall instrument. This combination of cost and size has so far prevented 3D laser nanoprinters to become anywhere close to as ubiquitous as graphical two-dimensional (2D) laser printers or other forms of optics-based 3D printers[12,19].

Here we introduce a photoresist system for 3D laser nanoprinting that contains benzil as a photoinitiator supporting two-step absorption instead of two-photon absorption. Two-step absorption is the reverse process of quantum cutting[20,21], whereas two-photon absorption is the reverse process of parametric downconversion[22]. We show that two-step absorption—if used under the appropriate conditions—exhibits the same crucial quadratic dependence of the exposure dose D on the light intensity I, that is, $D \propto I^2$, as two-photon absorption. Unlike for two-photon absorption, a continuous-wave (cw) laser with sub-milliwatt optical output power suffices for obtaining polymerization in two-step absorption. The actual exposure can require powers below 50 μW. Using a tiny semiconductor cw laser, which costs merely tens of euros, we demonstrate two-step absorption at laser wavelengths in the deep-blue spectral region. We describe the physics and chemistry of the two-step absorption

[1]Institute of Applied Physics, Karlsruhe Institute of Technology (KIT), Karlsruhe, Germany. [2]Institute of Nanotechnology, Karlsruhe Institute of Technology (KIT), Karlsruhe, Germany. [3]BioQuant, Universitätsklinikum, Ruprecht-Karls-Universität Heidelberg, Heidelberg, Germany. [4]Centre for Advanced Materials (CAM), Ruprecht-Karls-Universität Heidelberg, Heidelberg, Germany. [5]Institute of Organic Chemistry, Ruprecht-Karls-Universität Heidelberg, Heidelberg, Germany. ✉e-mail: vincent.hahn@kit.edu

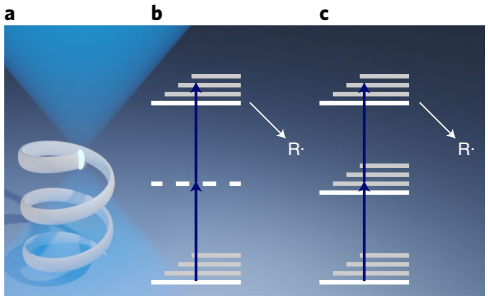

Fig. 1 | 3D laser nanoprinting using two-photon absorption or two-step absorption. a, Schematic of 3D laser nanoprinting based on a diffraction-limited laser focus for large numerical aperture (not to scale). **b**, Schematic of the energy-level diagram of a canonical two-photon absorption process exciting an electron from a photoinitiator ground state to an excited state with subsequent radical (R·) formation. The dashed horizontal line indicates the intermediate virtual state. **c**, The same energy-level diagram as in **b**, but for two-step absorption instead of two-photon absorption. Here a real intermediate electronic state is used instead of a virtual intermediate state in two-photon absorption.

process and demonstrate printing of selected benchmark 3D nanostructures. Some of these benchmarks go beyond the previous state-of-the-art values, even when including 3D laser nanoprinting enhanced by conceptually diffraction-unlimited stimulated emission depletion (STED)[18].

Two-step absorption versus two-photon absorption

In two-photon lithography (illustrated in Fig. 1b), an electron population of the initiator-molecule excited state starts a chemical reaction, which leads to the local crosslinking and hence the local solidification of a liquid monomer in a small volume element called the voxel[12] (analogous to a pixel—the 2D picture element). Under high-numerical-aperture (NA) focusing conditions, this voxel has a full-width at half-maximum (FWHM) of well below 1 µm in all three spatial dimensions[23]. Scanning of the laser focus according to a predefined path in three dimensions, as schematically illustrated in Fig. 1a, followed by a development process that washes out insufficiently cross-linked material, yields the wanted 3D micro- or nanostructure[7].

The basic idea of two-step absorption (Fig. 1c) is to replace the virtual state in two-photon absorption (Fig. 1b) by a real state, that is, by an intermediate electronic state that exists without the light field. Its lifetime is typically determined by non-radiative processes and can be orders of magnitude longer than femto- or picoseconds[24]. This difference implies three important aspects. First, the efficiency of converting two photons into an excited-state electron population increases with the ratio of the real-state lifetime to the virtual-state lifetime. This ratio can be extremely large. Second, the real-intermediate-state lifetime $\tau = k_D^{-1}$, the inverse of the real-intermediate-state decay rate, introduces a characteristic timescale into the overall process, which means that the exposure time is not scalable as that in ideal two-photon absorption. We illustrate the more complex behaviour of two-step absorption by the rate-equation calculations (Supplementary Information) for the simplified energy-level model shown in Fig. 2a. The cw excitation with intensity I starts at time $t=0$. The intensity enters into two transition rates, namely, $k_1 \propto \in_1 I$ and $k_2 \propto \in_2 I$, with extinction coefficients $\in_1$ and $\in_2$. We refer these rates and the time to k_D to obtain a universal representation. For early times (Fig. 2b), namely, $tk_D \ll 1$, the occupation of the upper level and hence the dose starts according to $D \propto t^2 I^2$. At times $tk_D \approx 10$, the behaviour follows $D \propto tI^2$. Note that for both regimes, the dose scales $\propto I^N$ with exponent $N=2$ (for comparison, $D \propto tI$ is expected for one-photon absorption and $D \propto tI^2$, for two-photon absorption). We calculate the general exponent from the logarithmic derivative as follows:

$$N = \frac{\mathrm{d}\log(D)}{\mathrm{d}\log(I)} = \frac{I}{D}\frac{\mathrm{d}D}{\mathrm{d}I}.$$

The dependence of N on k_1/k_D and k_2/k_D is shown in Fig. 2c, and the corresponding exposure time is shown in Fig. 2d. Figure 2e summarizes the dependence of I versus exposure time t_{exp} for a fixed dose of $D=0.1$ and $\in_2/\in_1 = 100$. This dependence is described in the experiments discussed below. Third, in two-step absorption, unlike for two-photon absorption, an electron in the intermediate state may already trigger a polymerization reaction. It is of utmost importance that we suppress such a trigger because this process would correspond to polymerization by ordinary one-photon absorption.

For benzil (Fig. 3a), the two-step-absorption photoinitiator molecule used in this work, a Jablonski energy diagram, based on another study[25], is depicted in Fig. 3b. As shown in Fig. 2a, the real intermediate-energy level shown in Fig. 1c is replaced by two nearby real intermediate levels, namely, the singlet S_1 state and triplet T_1 state. Intersystem crossing[24] brings electrons from the S_1 to T_1 state within a few nanoseconds[25]. The quantum efficiency of this non-radiative process is 92% (ref. [26]). Figure 3c shows the ground-state molar decadic extinction and excited-state extinction spectra of benzil in solution taken from the literature[27]. The wavelength of 405 nm (Fig. 3c, arrow) lies in the tail of both spectral maxima and therefore allows for mediating both types of transition. However, the ground-state extinction is about 100 times lower than triplet-state extinction[27]. This has two attractive consequences. First, at typical photoinitiator concentrations, the photoresist is sufficiently transparent over distances of ~300 µm, that is, over typical free-working distances of microscope objective lenses. This allows for dip-in 3D laser nanoprinting[28]. Second, due to the relatively high transient extinction, even moderate intensities are sufficient to promote a considerable fraction of triplet-excited molecules to a higher-excited triplet state.

For Norrish type I photoinitiators, radicals are generated by the fragmentation of molecules into radicals by cleaving chemical bonds[24], with typical bond energies above 3 eV (69 kcal mol^{-1} (ref. [29])). The triplet ground-state energy of benzil, $E_{T_1} = 2.3$ eV (54 kcal mol^{-1}), is well below that energy. For efficient bond scission from the triplet state, the triplet energy must be higher than the bond energy[29]. Hence, benzil has been referred to as a 'reluctant Norrish type I' initiator[29]—which has been our motivation for investigating benzil as a candidate for two-step absorption in the first place. However, benzil, as well as other α-diketones, readily abstracts hydrogen atoms from its triplet ground state[30]. This leads to an undesired one-photon-triggered polymerization reaction.

In addition to the two-step photoinitiator, the photoresists used here (subsequently abbreviated as PR1–PR4) contain bis(2,2,6,6-tetramethyl-4-piperidyl-1-oxyl) sebacate (BTPOS) (Supplementary Fig. 1) as a quencher and scavenger. BTPOS consists of two linked 2,2,6,6-tetramethyl-4-piperidyl-1-oxyl (TEMPO) moieties. Due to its persistent radical effect, TEMPO is commonly used in nitroxide-mediated radical polymerization[31]. Furthermore, TEMPO can suppress the undesired hydrogen abstraction initiated from an electron in the benzil triplet T_1 state[32], which may otherwise occur and lead to unwanted radicals initiating the polymerization reaction (Supplementary Fig. 2)[29]. This initiation would be based on a one-photon process. In addition, TEMPO favourably lowers the lifetime of the intermediate T_1 state[33]. Therefore, the concentration of TEMPO (or BTPOS) is a design parameter in the photoresist composition. Moreover, the photoresists PR1, PR2 and PR4 contain pentaerythritol triacrylate (PETA) as a monomer. Although the monomer contains a hydroxy group, which is prone

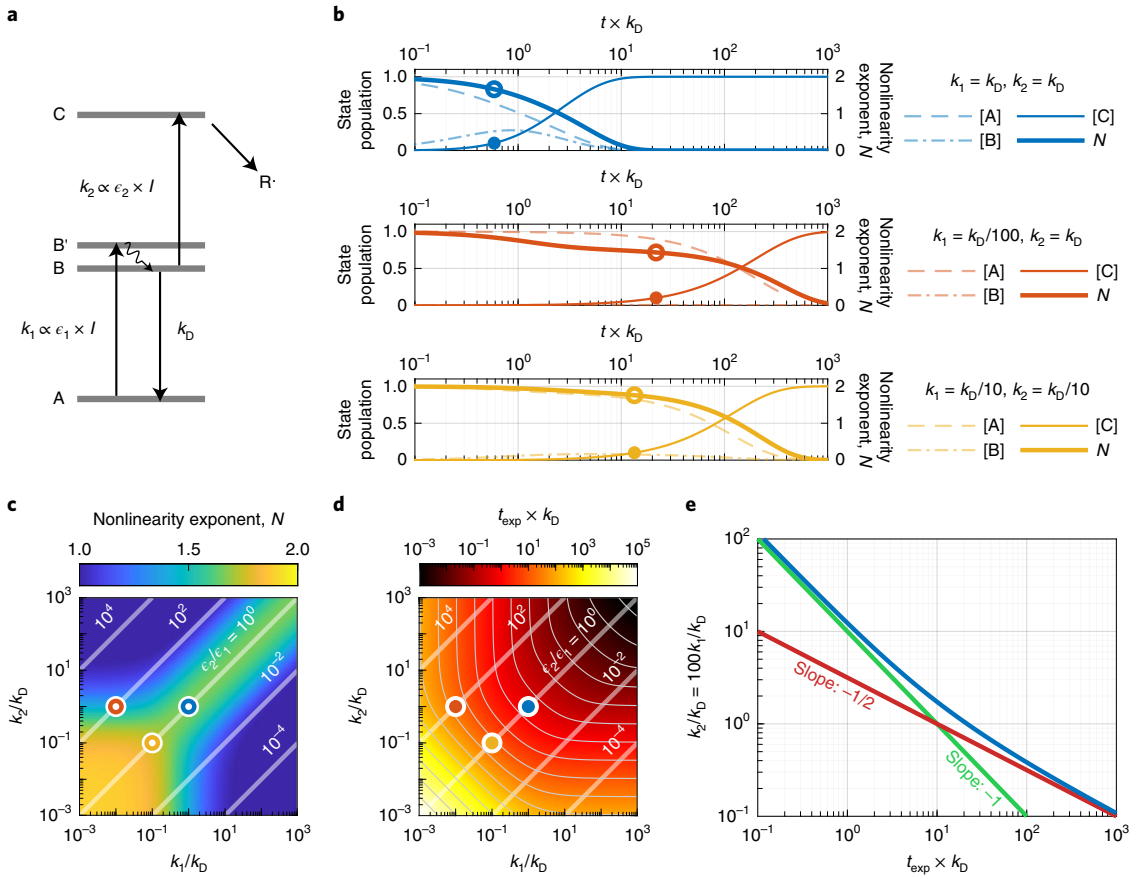

Fig. 2 | Simplified energy-level model and rate-equation calculations for a two-step-absorption photoinitiator. a, Energy levels, with ground state A, intermediate states B and B', and upper state C. We assume a rapid non-radiative decay from B' to B. Radicals (R·) are rapidly generated from a population of energy level C, leading to dose D. At $t = 0$, the ground-state population is 1, and all the other states are initially unpopulated. The rate coefficients $k_1 \propto \epsilon_1 I$ and $k_2 \propto \epsilon_2 I$ are proportional to the respective state's extinction coefficient and laser intensity I. **b**, Temporal evolution of the state population and the nonlinearity exponent N for three exemplary chosen parameter sets, as defined in the legends. The dots indicate the exposure time t_{exp} at which the threshold condition is met (we choose $D = 0.1$). For early times, the upper-state population increases according to $D \propto t^2 I^2$ (hence, $N = 2$). For $tk_D > 10$, we have $D \propto tI^2$ (hence, $N = 2$). **c**, Logarithmic false-colour plot of exponent N versus k_1/k_D and k_2/k_D. The straight white lines correspond to constant ratios ϵ_2/ϵ_1 as indicated. **d**, Normalized exposure time $t_{exp}k_D$ versus k_1/k_D and k_2/k_D. The encircled coloured points refer to the three conditions defined in **b**. **e**, Threshold intensity I, expressed in terms of k_2/k_D, versus $t_{exp}k_D$ for $D = 0.1$ and $\epsilon_2/\epsilon_1 = 100$.

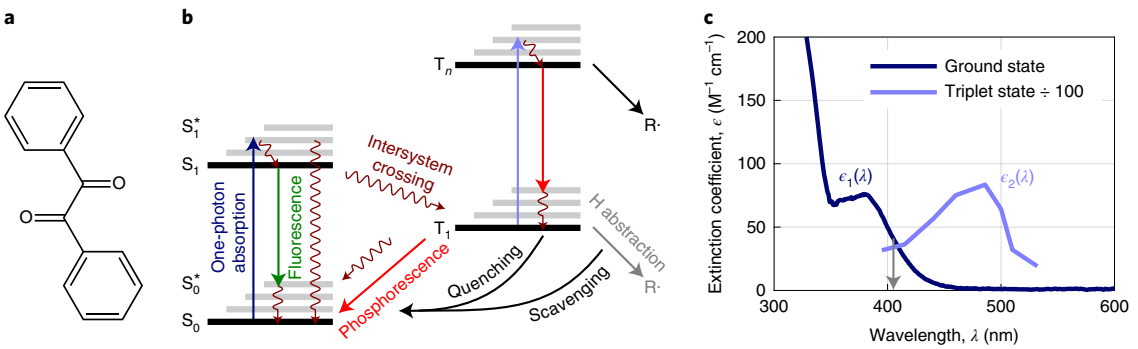

Fig. 3 | Benzil as a two-step-absorption photoinitiator. a, The benzil photoinitiator molecule used here. **b**, Corresponding Jablonski diagram. The real intermediate state in Fig. 1c is replaced by the excited-state singlet manifold, S1, and the ground-state triplet manifold, T1. As usual, intersystem crossing quickly brings electrons from S1 to T1. A scavenger (BTPOS) suppresses unwanted reactions starting from the occupation of the T1 state. The second step in two-step absorption (light blue) brings an electron from the T1 state to an excited triplet manifold T_n from where the radicals (R·) are generated, starting the polymerization reaction. **c**, Measured ground-state extinction (dark blue) and flash-photolysis triplet excitation spectra (light blue) of benzil in acetonitrile and benzene, respectively. Data for the latter spectrum have been taken from ref. [27].

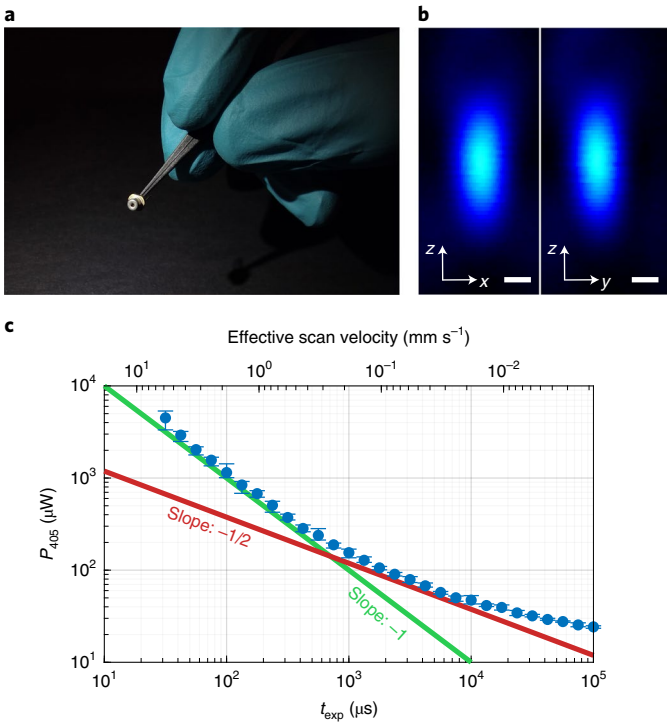

Fig. 4 | Laser, laser focus and effective nonlinearity of the photoresist. **a**, Photograph of the used semiconductor laser diode operating at 405 nm wavelength. **b**, Resulting laser focus as measured by scanning an 80-nm-diameter gold bead through the focus in three dimensions and detecting the scattered light. Cuts within the *x*–*z* and *y*–*z* plane are depicted; scale bars, 100 nm. The measured (squared) intensity FWHM values along the *x*, *y* and *z* directions are 163 nm (120 nm), 152 nm (113 nm) and 393 nm (288 nm), respectively. The used microscope objective lens has a NA of 1.4. **c**, Measured threshold laser power versus exposure time (dots) on a double-logarithmic scale for PR1. The straight red line has a slope of −1/2, and the green line has a slope of −1. The error bars mark the minimum and maximum values of at least three independent measurements.

to hydrogen abstraction[34], sufficient suppression of the photoinitiator triplet-state hydrogen-abstraction reaction by BTPOS could be achieved. In PR3, PETA was replaced by a similar monomer, namely, trimethylolpropane triacrylate (TMPTA), which does not possess a hydroxy group. For dip-in photoresist PR2, further components are added for refractive-index matching (Methods).

Results

To connect the behaviour of our photoresists with the modelling of two-step absorption (Fig. 2, particularly Fig. 2e), we have performed systematic point-exposure experiments (Methods) to investigate the dependence of threshold laser power $P=P_{th}$ (which, for fixed focusing conditions, is proportional to the threshold laser intensity I) and exposure time $t=t_{exp}$. The used semiconductor diode laser is shown in Fig. 4a. Here we focus the light with an oil-immersion microscope objective lens with NA of 1.4 (Methods). The measured laser focus is displayed in Fig. 4b. The aspect ratio of 2.5 of the axial- and lateral-intensity FWHM indicates a diffraction-limited laser focus. The results of the point-exposure experiments on two-step absorption are plotted as blue dots on a double-logarithmic scale (Fig. 4c). The straight lines with the indicated slopes are guides to the eye. The observed behaviour agrees with the behaviour for the energy-level model shown in Fig. 2e. In particular, we find a change in slope from −1/2 to −1 at an exposure time of $t_{exp}\approx 800\,\mu s$ or $t_{exp}k_D\approx 10$, corresponding to an intermediate-state lifetime of $\tau=k_D^{-1}\approx 80\,\mu s$. Outside the two-step-absorption model, this change in slope can be interpreted as being due to the transition from two-photon absorption to one-photon absorption[7]. However, in our two-step-absorption modelling discussed above, we have $N=2$ despite this change in slope. This means that our experimental findings are consistent with two-step absorption, but we cannot rule out one-photon absorption from these data alone.

In fact, in control experiments on photoinitiators for which it is established that one-photon absorption is observed at the considered wavelength, we find changes in the slope as well. Corresponding experiments for Irgacure 369 are shown in Supplementary Fig. 3. They were performed under otherwise similar conditions as the experiments using benzil as the photoinitiator (discussed below). We interpret the change in slope in Supplementary Fig. 3 as the onset of chemical nonlinearities in addition to one-photon absorption.

In general, one cannot draw conclusions from point-exposure experiments alone, regardless of the excitation mechanism. Consider the following example: a complex dense 3D structure requires many sequential point exposures. The tails of the laser focus excite the photoinitiator molecules in a volume that is much larger than that of the printed structure. This generally means that ingredients of the photoresist, especially oxygen, are locally irreversibly consumed during the printing process. Diffusion of these molecules leads to a global reduction in their density. Therefore, a single point exposure influences even other remote point exposures, giving rise to the proximity effect. Indeed, we are essentially unable to 3D print structures using Irgacure 369, as shown in Supplementary Fig. 4. We, therefore, discuss our 3D printing experiments using benzil.

In two dimensions, dense periodic line gratings (Fig. 5a) are an established benchmark structure to evaluate the spatial resolution[23,35] of a lithographic or printing approach. Resolution must not be confused with the minimum achievable line width of an isolated line[23,36]. In the experiments based on two-step absorption using 405 nm wavelength (Fig. 5b), we achieve the minimum grating period a or a resolution well below 150 nm, which surpasses previous best values obtained with STED-based multiphoton 3D laser nanoprinting at a fundamental wavelength of around 800 nm (ref. [23]). More importantly, in three dimensions, woodpile photonic crystals (Fig. 5c–e) with 24 layers along the z direction serve the same purpose[23] as line gratings in two dimensions. Each layer in this 3D stack is a simple line grating with period or pitch a in the x–y plane. Woodpiles are a demanding relevant benchmark because they contain a dense pattern that is periodic in all three dimensions. Therefore, possible accumulation or proximity effects arising from the tails of the tight laser focus (as mentioned earlier) are revealed—if they are problematic. No indications of severe proximity effects can be observed in the ultrathin section shown in Fig. 5e or in the corresponding 3D reconstructed volume (Supplementary Video 1). Furthermore, the quality and homogeneity of the woodpiles can be easily and intuitively assessed by their optical colour under white-light illumination in the reflection mode, as shown in Fig. 5c. We note that a laser power of ~45 μW used at a focus speed of $v=0.1\,mm\,s^{-1}$ (or 485 voxels s^{-1}, assuming a voxel size of 206 nm—the average size of the axial and lateral rod dimensions (Fig. 5e)) for the results shown in Fig. 5c–e are somewhat lower than that expected from point exposures (Fig. 4c) at that speed. This difference is due to the proximity effect in dense 3D woodpile structures (Fig. 5), which effectively lowers the polymerization threshold by about a factor of two with respect to the point exposures under these conditions. Summarizing the results shown in Fig. 5, the spatial resolution of 3D laser nanoprinting based on two-step absorption at 405 nm wavelength matches that of two-photon absorption combined with STED at about 800 nm wavelength[23].

In Fig. 6, we present a gallery of electron micrographs of other 3D-printed architectures. Some of these microstructures are

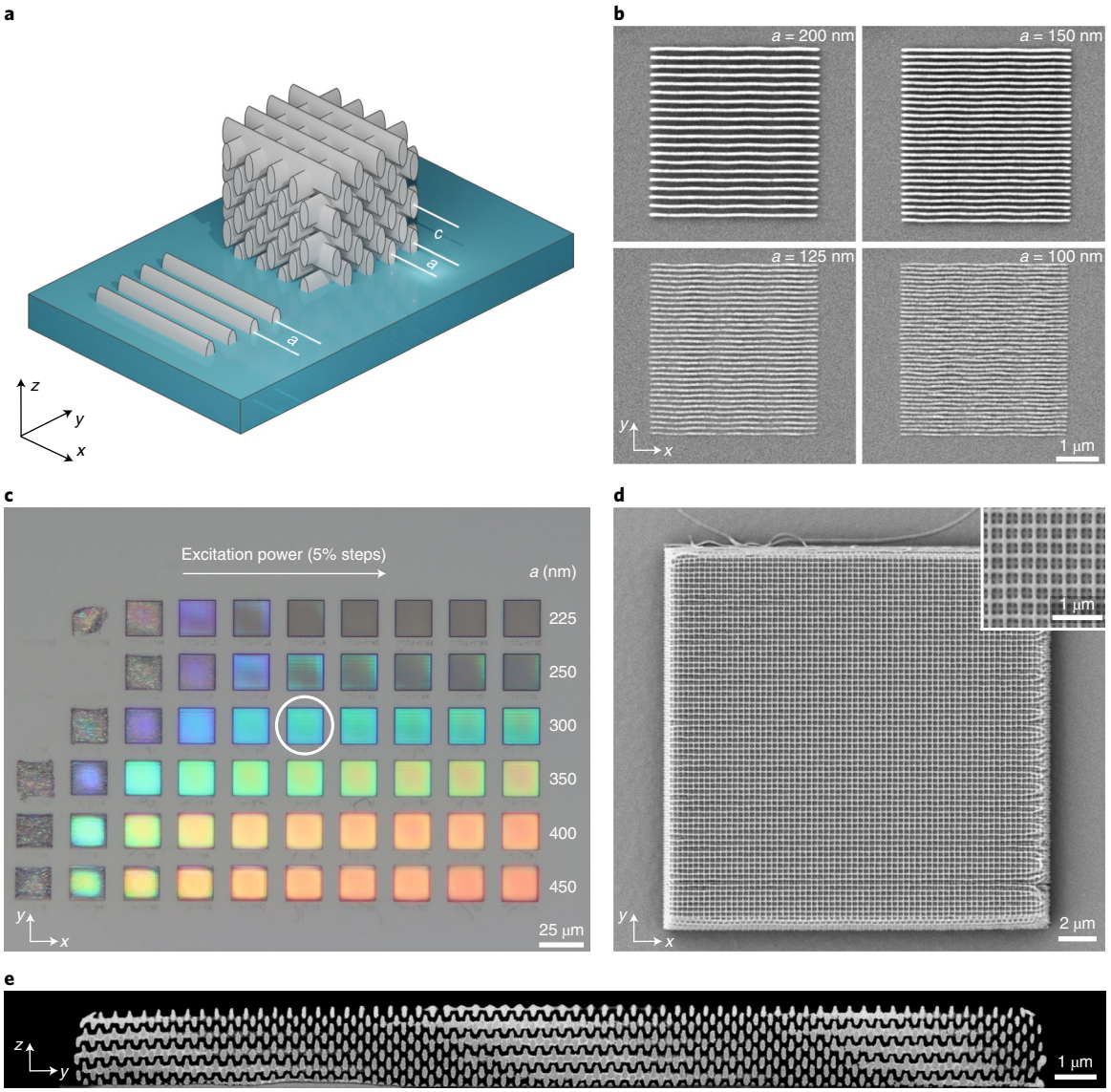

Fig. 5 | Two-step-absorption printing resolution in two and three dimensions. a, Schematic of 2D line grating with period a and a 3D woodpile structure, composed of stacked orthogonal layers of 2D line gratings with lateral period a and axial period $c = \sqrt{2}\,a$. **b**, Scanning electron micrograph of printed 2D line gratings. Periods below $a = 150$ nm are realized here. **c**, True-colour optical reflection-mode micrographs (NA of 0.4 for the objective lens) of a set of 3D woodpile structures. The used laser power is increased in steps of 5% in the horizontal direction. This (partly) leads to underexposed structures on the left and (partly) overexposed structures on the right. The rod spacing a is varied along the vertical direction. **d**, Top-view scanning electron micrograph of the woodpile with $a = 300$ nm (encircled). For comparison, the smallest rod spacing for 3D woodpiles made using two-photon absorption and near-infrared femtosecond lasers is 375 nm (ref. [23]) (without invoking STED). The corresponding commercial instrumentation allows high-quality 3D woodpile rod spacings not smaller than 500 nm (refs. [46,47]). All the displayed structures are 3D printed with a scan velocity $v = 0.1$ mm s^{-1} and using PR1. **e**, Scanning electron micrograph of an ultrathin section through a woodpile with rod spacing $a = 100$ nm. The cutting plane is tilted by 1.7° with respect to the 'crystallographic' y–z plane of the woodpile. We derive a rod and hence the voxel size along the y direction (z direction) of 110 nm (302 nm). A 3D reconstruction is shown in Supplementary Video 1. Both 2D and 3D results are consistent with the diffraction barrier imposed by the two-photon (or two-step) Sparrow criterion[23] (which is nearly identical to the FWHM of the squared intensity profile).

intentionally taller than the nanostructures shown in Fig. 5. Therefore, Fig. 6 shows that combining two-step absorption with the widespread immersion or dip-in[28] mode of 3D laser nanoprinting is readily possible. Clearly, dip-in 3D printing requires that the refractive index of two-step-absorption photoresist PR2 matches that underlying the design of the microscope objective lens (Methods and Supplementary Fig. 5). We note, however, that fast 3D printing of structures with a high filling fraction, as shown in Fig. 6e, is challenging for both PR2 and PR1. We attribute this to a higher concentration of abstractable hydrogen atoms within the used monomer. In Fig. 6, the printing laser-focus velocities are around 0.5–4.0 mm s^{-1} (or 2,400–19,400 voxels s^{-1}).

It is interesting to compare the scan speeds and laser powers used in two-step absorption with previous work on 3D laser printing using (quasi-)cw lasers exploiting one-photon absorption and chemical nonlinearities[37–40] or two-photon absorption[41]. Supplementary Fig. 8 compares these studies with the present one. Two-step absorption enables scan speeds that are up to three orders of magnitude faster than in previous studies, and (peak) laser powers that are up to three orders of magnitude lower. Furthermore,

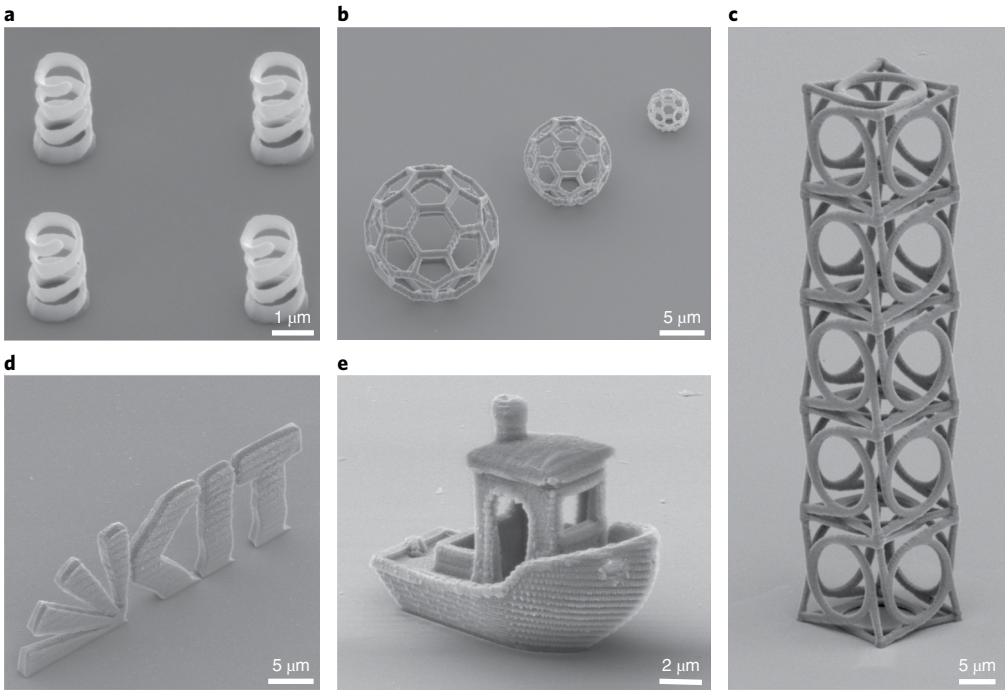

Fig. 6 | Gallery of oblique-view electron micrographs of further 3D-printed nanostructures. a, Helices with a radius of 800 nm and an axial pitch of 800 nm. **b**, Three buckyball models with diameters of 15, 10 and 5 µm. **c**, Five stacked chiral metamaterial unit cells[48] with a lattice constant of 16 µm. **d**, Three-dimensional model of the logo of the Karlsruhe Institute of Technology. **e**, Miniaturized model of the #3DBenchy structure[49]. Detailed 3D printing parameters for all the structures are provided in Supplementary Table 1.

we achieve a spatial resolution that is far superior to most of these and that matches the previous best results using STED-inspired two-photon 3D laser nanoprinting[23].

Concluding remarks

We have introduced two-step absorption in benzil replacing two-photon absorption as the fundamental photoinitiation mechanism in 3D laser nanoprinting. The presented 2D and 3D benchmark nanostructures match or even surpass previous results obtained with two-photon absorption in terms of achievable spatial resolution. More importantly, our two-step-absorption results were obtained with a cw semiconductor laser diode that is many orders of magnitude less expensive and smaller in volume than the femtosecond lasers commonly used today for obtaining efficient two-photon absorption. Moreover, for two-step absorption, we have not once observed an indication of micro-explosions. Unwanted photoresist micro-explosions typically occur every day when using two-photon absorption and femtosecond pulses in 3D laser nanoprinting.

We consider two-step absorption replacing two-photon absorption in 3D laser nanoprinting as a breakthrough. First, it paves the way for cutting down the cost of future 3D laser nanoprinters by several orders of magnitude—in addition to maintaining and even surpassing the accessible spatial resolution, although currently at lower peak printing rates than the best values obtained for two-photon absorption[12]. Second, a dramatic miniaturization of 3D laser nanoprinters is straightforward, given that the diode laser used here has a volume of only some cubic millimetres. Combined, the drastic reduction in cost and size will likely dramatically amplify the spread of 3D laser nanoprinters in the academic field in the upcoming years. Third, by combining STED and two-step absorption, the achievable spatial resolution could be further improved, even beyond the diffraction barrier. Fourth, the replacement of one-photon absorption by two-step absorption could improve the spatial resolution in computed axial lithography[42–44]. Furthermore, two-step absorption with two different laser colours is a prerequisite for light-sheet 3D laser printing[45]. Both have the potential to boost the 3D printing speed.

Online content

Any methods, additional references, Nature Research reporting summaries, source data, extended data, supplementary information, acknowledgements, peer review information; details of author contributions and competing interests; and statements of data and code availability are available at https://doi.org/10.1038/s41566-021-00906-8.

Received: 20 May 2021; Accepted: 29 September 2021;
Published online: 29 November 2021

References

1. Göppert-Mayer, M. Über Elementarakte mit zwei Quantensprüngen. *Ann. Phys.* **401**, 273–294 (1931).
2. Scully, M. O. & Zubairy, M. S. *Quantum Optics* (Cambridge Univ. Press, 1997).
3. Denk, W., Strickler, J. H. & Webb, W. W. Two-photon laser scanning fluorescence microscopy. *Science* **248**, 73–76 (1990).
4. Denk, W., Piston, D. W. & Webb, W. W. Multi-photon molecular excitation in laser-scanning microscopy. in *Handbook Of Biological Confocal Microscopy* (ed. Pawley, J. B.) 535–549 (Springer, 2006).
5. Wu, E.-S., Strickler, J. H., Harrell, W. R. & Webb, W. W. Two-photon lithography for microelectronic application. In *Proc. SPIE 1674, Optical/Laser Microlithography V* 776–782 (International Society for Optics and Photonics, 1992).
6. Maruo, S., Nakamura, O. & Kawata, S. Three-dimensional microfabrication with two-photon-absorbed photopolymerization. *Opt. Lett.* **22**, 132–134 (1997).
7. Baldacchini, T. (ed.) *Three-Dimensional Microfabrication Using Two-Photon Polymerization* 2nd edn (Elsevier, 2019).
8. Farsari, M. & Chichkov, B. N. Two-photon fabrication. *Nat. Photon.* **3**, 450–452 (2009).
9. Gissibl, T., Thiele, S., Herkommer, A. & Giessen, H. Two-photon direct laser writing of ultracompact multi-lens objectives. *Nat. Photon.* **10**, 554–560 (2016).

10. Dietrich, P.-I. et al. In situ 3D nanoprinting of free-form coupling elements for hybrid photonic integration. *Nat. Photon.* **12**, 241–247 (2018).
11. Wolff, M. A. et al. Broadband waveguide-integrated superconducting single-photon detectors with high system detection efficiency. *Appl. Phys. Lett.* **118**, 154004 (2021).
12. Hahn, V. et al. Rapid assembly of small materials building blocks (voxels) into large functional 3D metamaterials. *Adv. Funct. Mater.* **30**, 1907795 (2020).
13. Skliutas, E. et al. Polymerization mechanisms initiated by spatio-temporally confined light. *Nanophotonics* **10**, 1211–1242 (2021).
14. Kiefer, P. et al. Sensitive photoresists for rapid multiphoton 3D laser micro- and nanoprinting. *Adv. Opt. Mater.* **8**, 2000895 (2020).
15. Schafer, K. J. et al. Two-photon absorption cross-sections of common photoinitiators. *J. Photochem. Photobiol. Chem.* **162**, 497–502 (2004).
16. Pawlicki, M., Collins, H. A., Denning, R. G. & Anderson, H. L. Two-photon absorption and the design of two-photon dyes. *Angew. Chem. Int. Ed.* **48**, 3244–3266 (2009).
17. Mueller, J. B., Fischer, J., Mange, Y. J., Nann, T. & Wegener, M. In-situ local temperature measurement during three-dimensional direct laser writing. *Appl. Phys. Lett.* **103**, 123107 (2013).
18. Fischer, J. et al. Three-dimensional multi-photon direct laser writing with variable repetition rate. *Opt. Express* **21**, 26244–26260 (2013).
19. Tumbleston, J. R. et al. Continuous liquid interface production of 3D objects. *Science* **347**, 1349–1352 (2015).
20. Dexter, D. L. Possibility of luminescent quantum yields greater than unity. *Phys. Rev.* **108**, 630–633 (1957).
21. Wegh, R. T., Donker, H., Oskam, K. D. & Meijerink, A. Visible quantum cutting in $LiGdF_4:Eu^{3+}$ through downconversion. *Science* **283**, 663–666 (1999).
22. Burnham, D. C. & Weinberg, D. L. Observation of simultaneity in parametric production of optical photon pairs. *Phys. Rev. Lett.* **25**, 84–87 (1970).
23. Fischer, J. & Wegener, M. Three-dimensional direct laser writing inspired by stimulated-emission-depletion microscopy. *Opt. Mater. Express* **1**, 614–624 (2011).
24. Turro, N. J. *Modern Molecular Photochemistry* (University Science Books, 1991).
25. Flamigni, L., Barigelletti, F., Dellonte, S. & Orlandi, G. Photophysical properties of benzil in solution: triplet state deactivation pathways. *J. Photochem.* **21**, 237–244 (1983).
26. Lamola, A. A. & Hammond, G. S. Mechanisms of photochemical reactions in solution. XXXIII. Intersystem crossing efficiencies. *J. Chem. Phys.* **43**, 2129–2135 (1965).
27. Fang, T.-S., Brown, R. E., Kwan, C. L. & Singer, L. A. Photophysical studies on benzil. Time resolution of the prompt and delayed emissions and a photokinetic study indicating deactivation of the triplet by reversible exciplex formation. *J. Phys. Chem.* **82**, 2489–2496 (1978).
28. Bückmann, T. et al. Tailored 3D mechanical metamaterials made by dip-in direct-laser-writing optical lithography. *Adv. Mater.* **24**, 2710–2714 (2012).
29. Scaiano, J. C., Johnston, L. J., McGimpsey, W. G. & Weir, D. Photochemistry of organic reaction intermediates: novel reaction paths induced by two-photon laser excitation. *Acc. Chem. Res.* **21**, 22–29 (1988).
30. Cáceres, T., Encinas, M. V. & Lissi, E. A. Photocleavage of benzil. *J. Photochem.* **27**, 109–114 (1984).
31. Grubbs, R. B. Nitroxide-mediated radical polymerization: limitations and versatility. *Polym. Rev.* **51**, 104–137 (2011).
32. Johnston, L. J., Tencer, M. & Scaiano, J. C. Evidence for hydrogen transfer in the photochemistry of 2,2,6,6-tetramethylpiperidine *N*-oxyl. *J. Org. Chem.* **51**, 2806–2808 (1986).
33. Tatikolov, A. S., Levin, P. P., Kokrashvili, T. A. & Kuz'min, V. A. Quenching of the triplet states of carbonyl compounds by nitroxyl radicals. *Russ. Chem. Bull.* **32**, 465–468 (1983).
34. Bunbury, D. L. & Chuang, T. T. Photolysis of benzil in 2-propanol and in cumene. *Can. J. Chem.* **47**, 2045–2055 (1969).
35. Arnoux, C. et al. Polymerization photoinitiators with near-resonance enhanced two-photon absorption cross-section: toward high-resolution photoresist with improved sensitivity. *Macromolecules* **53**, 9264–9278 (2020).
36. Malinauskas, M. et al. Ultrafast laser processing of materials: from science to industry. *Light: Sci. Appl.* **5**, e16133 (2016).
37. Ikuta, K., Maruo, S. & Kojima, S. New micro stereo lithography for freely movable 3D micro structure-super IH process with submicron resolution. In *Proc. MEMS 98. IEEE. Eleventh Annual International Workshop on Micro Electro Mechanical Systems. An Investigation of Micro Structures, Sensors, Actuators, Machines and Systems (Cat. No. 98CH36176)* 290–295 (IEEE, 1998).
38. Thiel, M., Fischer, J., von Freymann, G. & Wegener, M. Direct laser writing of three-dimensional submicron structures using a continuous-wave laser at 532 nm. *Appl. Phys. Lett.* **97**, 221102 (2010).
39. Do, M. T. et al. Submicrometer 3D structures fabrication enabled by one-photon absorption direct laser writing. *Opt. Express* **21**, 20964–20973 (2013).
40. Delrot, P., Loterie, D., Psaltis, D. & Moser, C. Single-photon three-dimensional microfabrication through a multimode optical fiber. *Opt. Express* **26**, 1766–1778 (2018).
41. Mueller, P., Thiel, M. & Wegener, M. 3D direct laser writing using a 405 nm diode laser. *Opt. Lett.* **39**, 6847–6850 (2014).
42. Shusteff, M. et al. One-step volumetric additive manufacturing of complex polymer structures. *Sci. Adv.* **3**, eaao5496 (2017).
43. Kelly, B. E. et al. Volumetric additive manufacturing via tomographic reconstruction. *Science* **363**, 1075–1079 (2019).
44. Loterie, D., Delrot, P. & Moser, C. High-resolution tomographic volumetric additive manufacturing. *Nat. Commun.* **11**, 852 (2020).
45. Regehly, M. et al. Xolography for linear volumetric 3D printing. *Nature* **588**, 620–624 (2020).
46. Schumann, M. F. et al. Cloaked contact grids on solar cells by coordinate transformations: designs and prototypes. *Optica* **2**, 850–853 (2015).
47. Urbancová, P. et al. IP-Dip-based woodpile structures for VIS and NIR spectral range: complex PBG analysis. *Opt. Mater. Express* **9**, 4307–4317 (2019).
48. Frenzel, T., Kadic, M. & Wegener, M. Three-dimensional mechanical metamaterials with a twist. *Science* **358**, 1072–1074 (2017).
49. #3DBenchy. https://www.3dbenchy.com/

Methods

Photoresist composition and handling. Benzil (98%) was purchased from Aldrich. BTPOS (98%) was purchased from TCI Chemicals. A ground-state extinction spectrum is shown in Supplementary Fig. 7. PETA was purchased from Sigma-Aldrich. IP-Dip NPI (no photoinitiator) was purchased from Nanoscribe. TMPTA (93%) was purchased from Alfa Aesar. Irgacure 369 was purchased from Ciba Specialty Chemicals.

The four different photoresist systems used here are named PR1–PR4 and are described below.

PR1: Benzil (21.0 mg, 100 µmol) and BTPOS (25.6 mg, 50 µmol) are dissolved in 1 ml PETA. This corresponds to 1.7 wt% benzil and 2.1 wt% BTPOS. The mixture is stirred on a hot plate at a temperature of 45 °C for 4 h until all the compounds have dissolved.

PR2: Benzil (21.0 mg, 100 µmol) and BTPOS (25.6 mg, 50 µmol) are dissolved in a 1 ml mixture of IP-Dip NPI and PETA (70 vol% and 30 vol%). This corresponds to 1.8 wt% benzil and 2.2 wt% BTPOS. The ratio of IP-Dip NPI and PETA is chosen to obtain a diffraction-limited focus (Supplementary Fig. 5). The mixture is stirred on a hot plate at a temperature of 45 °C for 4 h until all the compounds have dissolved.

PR3: Benzil (21.0 mg, 100 µmol) and BTPOS (25.6 mg, 50 µmol) are dissolved in 1 ml TMPTA. This corresponds to 1.8 wt% benzil and 2.2 wt% BTPOS. The mixture is stirred on a hot plate at a temperature of 45 °C for 4 h until all the compounds have dissolved.

PR4: Irgacure 369 (18.3 mg, 50 µmol) and BTPOS (12.8 mg, 25 µmol) are dissolved in 1 ml PETA. This corresponds to 1.5 wt% Irgacure 369 and 1.1 wt% BTPOS. The mixture is stirred on a hot plate at a temperature of 40 °C for 8 h until all the compounds have dissolved. The solubility of the Irgacure initiator was lower than that of benzil. The relative concentration of BTPOS was chosen to be constant. All the photoresists were mixed and polymerized under yellow-light conditions.

3D printing setup. The laser diode (L405P150, Thorlabs) is mounted on a temperature-controlled mount (LDM56/M, Thorlabs). A spectrum of the laser emission is displayed in Supplementary Fig. 6. The diode's temperature is controlled by a thermoelectric cooler controller (TED200C, Thorlabs) and the electrical current is controlled using a laser diode driver (LDC200, Profile). An aspheric 8-mm-focal-length collimator lens (A240TM-A, Thorlabs) collimates the laser diode output. The laser diode's beam is focused using a 40-mm-focal-length plano-convex (LA1422-A, Thorlabs) lens through a 10-µm-diameter pinhole (P10C, Thorlabs) and collimated by a 75-mm-focal-length achromatic lens (AC254-075-A, Thorlabs). The beam is deflected by a pair of galvanometric mirrors (Saturn 5B 56S, Pangolin Laser Systems) that are imaged by two achromatic lenses (ACL254-100-A and ACL254-150-A, Thorlabs) through a quarter-wave plate (WPQSM05-405, Thorlabs) on the entrance pupil of a microscope objective lens (HCX PL APO 100×/1.4–0.7 Oil CS, Leica Microsystems). For 3D printing the woodpile structures, no quarter-wave plate was used. The objective lens focuses the beam into the sample photoresist (25 µl), which, for non-dip-in experiments, is contained in a polydimethylsiloxane (PDMS) ring (5 mm diameter) placed on a methacrylate silanized glass coverslip (no. 1.5H, Paul Marienfeld). The coverslip is mounted on a 3D piezoelectric stage (P-527.3CL, Physik Instrumente). For 3D printing the structures shown in Fig. 6c,e, the piezoelectric stage was replaced by one with a larger travel range (P-563.3CD, Physik Instrumente). Galvanometric x–y scanning was used for all the 3D structures shown in Fig. 6. All the other structures were 3D printed by scanning the sample with piezoelectrically actuated stages.

During 3D printing, the sample is illuminated using an LED with a peak wavelength $\lambda \approx 640$ nm and observed in situ in the transmission mode on a charge-coupled device camera.

The laser power was adjusted using a half-wave plate (WPHSM05-405, Thorlabs) and a polarizing beamsplitter cube (PBS251, Thorlabs), both located in front of the galvanometric mirror pair. To probe the exposure powers even below the lowest possible power setting permitted by the half-wave plate and beamsplitter, absorptive neutral-density glass filters (FSQ-OD20 to FSQ-OD300, Coherent) were placed behind the polarizing beamsplitter cubes. The laser focus was routinely checked to ensure that the filter glass does not cause any wavefront aberrations.

All the laser power values were measured at the entrance pupil of the objective lens using a semiconductor sensor (TP86, Coherent). For the point-exposure measurements, the pulses were monitored using an avalanche photodiode (APD410A/M, Thorlabs) placed at the idle output of the polarizing beamsplitter cube.

Detailed printing parameters for all the displayed 3D structures are given in Supplementary Table 1.

Sample development. All the samples, except the woodpile photonic crystals, were developed by immersing the sample for 3 min in a bath of acetone (ultraviolet/infrared (UV/IR) grade) and a subsequent wash in 2-propanol (UV/IR grade). The samples were then blow-dried in a gentle stream of nitrogen.

The woodpile photonic crystals were developed in acetone (UV/IR grade) with subsequent supercritical drying in CO_2 using EM CPD300 (Leica Microsystems).

Extinction spectra. The extinction spectra were recorded in spectroscopy-grade acetonitrile in a quartz cuvette using a Cary 300 (Agilent Technologies) spectrometer.

Generation of cross sections from woodpile photonic crystals. Arrays of woodpile photonic crystals were incubated for 2 h with 2% OsO_4 in acetone, infiltrated for 3 h with 50% Epon in acetone, embedded in 100% Epon (consisting of 42.4 g glycid ether 100, 29.6 g dodecenylsuccinic acid anhydride, 18.4 g methyl-5-norbornene-2,3-dicarboxylic anhydride and 2.4 g benzyldimethylamine; all chemicals were purchased from SERVA) and polymerized for 2 days at 62 °C. After removal of the glass coverslip by insertion in liquid nitrogen, the resin blocks were trimmed to expose the target row of woodpiles. Ultrathin (80 nm) cross sections were cut using a PowerTome PC ultramicrotome (RMC Boeckeler) and placed on pieces of silicon wafer. They were imaged in a field-emission scanning electron microscope (Ultra 55, Carl Zeiss Microscopy) at a primary electron energy of 1.5 keV. Large scan fields were recorded using the Atlas 5 Array Tomography software and the energy-selective detector for back-scattered electrons.

Data availability

The data underlying the plots within this paper, Supplementary Information and related 3D printing files are published on the open-access data repository of the Karlsruhe Institute of Technology (https://doi.org/10.5445/IR/1000137134).

Code availability

The code for the computations shown in Fig. 2 is published on the open-access data repository of the Karlsruhe Institute of Technology (https://doi.org/10.5445/IR/1000137134).

Acknowledgements

We acknowledge fruitful discussions with C. Barner-Kowollik (Queensland Institute of Technology), F. Mayer (Karlsruhe Institute of Technology (KIT)), P. Müller (previously at KIT) and T. Schlöder (KIT). V.H. is presently funded by the Max Planck School of Photonics. This research has additionally been funded by the Deutsche Forschungsgemeinschaft (DFG, German Research Foundation) under Germany's Excellence Strategy via the Excellence Cluster '3D Matter Made to Order' (EXC-2082/1-390761711), which has also been supported by the Carl Zeiss Foundation through the 'Carl Zeiss Foundation-Focus@HEiKA', by the State of Baden-Württemberg, and by KIT. We further acknowledge support by the Helmholtz program 'Materials Systems Engineering (MSE)', and by the Karlsruhe School of Optics & Photonics (KSOP) and by the Ministry of Science, Research and the Arts of Baden-Württemberg as part of the sustainability financing of the projects of the Excellence Initiative II. R.R.S. acknowledges funding from the Federal Ministry for Education and Research (BMBF) under grant no. 13N14476.

Author contributions

V.H. and M.W. had the idea to use two-step absorption instead of two-photon absorption. V.H. screened possible photoinitiator candidates suitable for two-step absorption. V.H., T.M. and N.M.B. performed all the experiments and the corresponding analysis. E.R.C. and I.W. performed the sample preparation, ultramicrotomy and electron microscopy of the cross sections. R.R.S. prepared the 3D reconstruction of the woodpile structures. M.W. and E.B. supervised the project. M.W. drafted the first version of the paper. All the authors contributed to the interpretation of the results and writing of the manuscript.

Competing interests

V.H., T.M. and M.W. are inventors on a patent application on two-step absorption. The authors declare no other competing interests.

Additional information

Supplementary information The online version contains supplementary material available at https://doi.org/10.1038/s41566-021-00906-8.

Correspondence and requests for materials should be addressed to Vincent Hahn.

Peer review information *Nature Photonics* thanks Paul Braun and the other, anonymous, reviewer(s) for their contribution to the peer review of this work.

Reprints and permissions information is available at www.nature.com/reprints.